Small scale spatial variability of bare-ice reflectance at Jamtalferner, Austria

Lea Hartl (1), Lucia Felbauer (1), Gabriele Schwaizer (2), Andrea Fischer (1)

1) Institute for Interdisciplinary Mountain Reasearch, Austrian Academy of Sciences, Technikerstraße, 21a, ICT, 6020 Innsbruck, Austria
2) ENVEO GmbH, Fürstenweg 176, 6020 Innsbruck, Austria

**Abstract**

As Alpine glaciers become snow free in summer, more dark, bare ice is exposed, decreasing local albedo and increasing surface melting. To include this feedback mechanism in models of future deglaciation, it is important to understand the processes governing broadband and spectral albedo at a local scale. However, little in situ reflectance data has been measured in the ablation zones of mountain glaciers. As a contribution to this knowledge gap, we present spectral reflectance data (Hemispherical-Conical-Reflectance-Factor) from 325 to 1075 nm collected along several profile lines in the ablation zone of Jamtalferner, Austria. Measurements were timed to closely coincide with a Sentinel-2 and Landsat-8 overpass and are compared to the respective ground reflectance (Bottom-Of-Atmosphere) products. The brightest spectra have a maximum reflectance of up to 0.7 and consist of clean, dry ice. In contrast, reflectance does not exceed 0.2 for dark spectra where liquid water and/or fine-grained debris are present. Spectra can roughly be grouped into dry ice, wet ice, and dirt/rocks, although gradations between these groups occur. Neither satellite captures the full range of in situ reflectance values. The difference between ground and satellite data is not uniform across satellite bands, between Landsat and Sentinel, and to some extent between ice surface types (underestimation of reflectance for bright surfaces, overestimation for dark surfaces). We highlight the need for further, systematic measurements of in situ spectral reflectance properties, their variability in time and space, and in- depth analysis of time-synchronous satellite data.

**1. Introduction**
**1.1 General context and aims**
Under ongoing climate change, mountain glaciers are retreating at unprecedented rates (Zemp et al, 2015, 2019). Glaciers in the Eastern Alps are losing mass rapidly, and due to persistent loss of snow cover exposing the underlying firn (Fischer, 2011), many have lost much of their firn cover. An increasing amount of darker bare ice is exposed in Summer and at some glacier tongues, darkening of the ice has been observed (Klok et al., 2003). These feedback mechanisms in turn increase the amount of energy absorbed and accelerate melt (e.g. Paul et al., 2005; Box et al., 2012; Naegeli et al., 2017 & 2019). The reflective properties of glacier ice are affected by e.g. the absence or presence and amount of dust, pollen, debris, cryoconite, supraglacial water, and biota including local production rates (Dumont et al., 2009; Gabbi et al. 2015; Azzoni et al., 2016). Variability is understood to be high, but few measurements and models exist. In a glaciological context, the spatial and temporal variability of ice albedo is understudied compared to snow albedo.

We present spectroradiometric data on the spatial variability of bare-ice reflectance at the tongue of Jamtalferner, Austria, aiming to contribute to closing the knowledge gap in bare ice variability as an important feedback mechanism in glacier mass loss. Specifically, we aim to:

1) Provide a first-order quantitative assessment of spatial variability of surface reflectance in the ablation area of the rapidly melting Jamtalferner, quantifying possible ranges of spectral reflectance and qualitatively summarizing different surface types.
2) Compare commonly used reflectance products derived from Landsat-8 and Sentinel-2 data with in situ measurements, highlighting areas in which further study is required if ongoing processes related to deglaciation are to be fully captured by satellite data.

**1.2 In situ and remote sensing-based change detection of surface reflectance properties of glacier ice**

In the following section we summarize previous studies on this topic. For clarity, we begin with a note on terminology: Following the definitions and guidelines detailed in Schaepman-Strub et al., (2004, 2006) and Nicodemus et al. (1977), we use the term "albedo" for bihemispherical reflectance (BHR), including cases where this parameter is approximately measured with an albedometer. In situ measurements with field spectrometers – such as they were carried out for this study – generally represent Hemispherical-Conical-Reflectance-Factors (HCRF). For exact specifications of what is represented by satellite derived surface reflectance products we refer to the documentation of the respective products as this differs between sensors and product suites.

61 While it is generally understood that albedo is a major driving factor for the energy balance and radiative regime of
62 glaciers, few studies discuss ice albedo and its variability at the local level. Early investigations of ice albedo were
63 carried out by Sauberer in 1938. Building on this work, Sauberer and Dirmhirn (1951) showed that albedo is highly
64 variable in time and space and strongly affects the radiation balance. They reported mean values of 0.37 for clean ice
65 and 0.13 for dirty ice at Sonnblick glacier (Austria), a pronounced diurnal cycle of albedo related to refreezing of the
66 surface, and influence of wind transported fine mineral dust. In another study based on measurements at Sonnblick, they
67 highlighted that the collection of mineral dust in cryoconite holes affects albedo, as does liquid water, and showed a
68 diurnal reduction of albedo of about 0.2 under clear sky conditions, which they attribute to melt-freeze cycles on the ice
69 surface (Sauberer and Dirmhirn, 1952). Jaffé (1960) also pointed out the importance of cryoconite and air content in the
70 upper most ice layer for the radiative properties. Dirmhirn and Trojer (1955) presented a histogram-like curve of the
71 frequency of different ice albedo values measured on the tongue of Hintereisferner (Austria): Broadband ice albedo
72 ranges from <0.1 to about 0.58, with a frequency maximum at 0.28. Similar to the results from Sonnblick, melt-related
73 diurnal albedo variations were also found at Hintereisferner. In a detailed study of the radiation balance at
74 Hintereisferner, Hoinkes and Wendler (1968) showed the importance of summer snow falls for albedo, as well as
75 seasonal changes in ice albedo, and their significant contribution to ablation.
76
77 Considering the growing dominance of bare ice areas both compared to overall glacier area and in terms of glacier-wide
78 mass- and energy balance, the sensitivity of the latter parameters to changing reflectance properties has become of
79 increasing interest throughout approximately the last decade. Using a combination of mass balance data from multiple
80 Swiss glaciers and the Landsat-8 surface reflectance product, Naegeli and Huss (2015) show that mass balance
81 decreases on average by 0.14 m w.e. a−1 per 0.1 albedo decrease. In order to better delineate associated driving
82 processes at the glacier surface, it is important to assess reflectance properties not only as broadband albedo at the scale
83 of a glacier, but at a high spectral and spatial resolution. A number of studies attribute recent darkening of European
84 glaciers to increased accumulation of mineral dust (e.g. Oerlemans et al., 2009, Azzoni et al., 2016) and black carbon
85 (e.g. Painter et al., 2013, Gabbi et al., 2015). Similar findings have been reported from the Himalayas (e.g. Ming et al.
86 2012, 2015; Qu et al. 2014) and the Greenland ice sheet (Dumont et al., 2009). Some discussion remains as to whether
87 the observed darkening is primarily due to the increase of bare ice areas compared to overall glacier area, or whether
88 there is a darkening of the bare ice areas as such, and if so, whether bare ice areas are darkening due to local processes
89 or large scale systemic change (e.g. Box et al., 2012; Alexander et al., 2014; Naegeli, 2019).
90
91 Different methodological approaches have been used to address specific changes in the surface characteristics of the
92 ablation zone as they relate to changes in reflectance properties and energy absorption across the electromagnetic
93 spectrum: Using both hyperspectral satellite data and in situ HCRF measurements, Di Mauro et al. (2017) find that the
94 presence of elemental and organic carbon leads to darkening of the ablation zone at Vadret da Morteratsch (Switzerland)
95 and discuss potential anthropogenic contributions. Azzoni et al. (2016) use semi-automatic image analysis techniques
96 on photos of the ice surface at Forni glacier (Italy) to quantify the amount of fine debris present on the surface and its
97 effect on the albedo. They find an overall darkening due to increasing dust, as well as significant effects of melt and rain
98 water. Naegeli et al. (2015) use in situ spectrometer and airborne image spectroscopy data with a pixel resolution of
99 approximately 2m to classify glacier surface types and map spectral albedo on Glacier de la Plaine Morte in
100 Switzerland. Additionally, they highlight the difference in scale between albedo variability at the ice surface and the
101 pixel resolution of satellite data and the need for detailed case studies combining ground truth data and remote sensing
102 techniques to bridge this gap. In situ data is also essential for model verification, as shown e.g. by Malinka et al. (2016),
103 who use reflectance spectra (HCRF) gathered on sea ice to validate modelled reflectance parameters.
104
105 In order to scale assessments of ice albedo from the local to a regional or global level, satellite-derived data are
106 indispensable. Earlier in the satellite era, several studies carried out comparisons of albedo data measured on the ground
107 and surface reflectance derived from Landsat-5 Thematic Mapper scenes, finding considerable differences between in
108 situ and satellite data especially in the ablation area (e.g. Hall et al., 1989 & 1990; Koelemeijer et al., 1993; Winther,
109 1993; Knap et al., 1999). These works are mostly based on albedo data from a single location, such as an automatic
110 weather station (AWS), and it was often not possible to carry out ground measurements so that they coincided with the
111 satellite overpasses. More recently, Brun et al. (2015) highlight the importance of remote sensing data for monitoring of
112 glacier albedo changes in remote regions where data collection on the ground is impossible or impractical and compare
113 MODIS data with in situ radiation measurements. Albedo measurements from AWS sites on the Greenland ice sheet –
114 associated with the PROMICE and GC-Net monitoring networks - have been used to improve gridded albedo products
115 based on MODIS data, showing the importance of using ground truth in conjunction with satellite data (Box et al.,
116 2013; van As et al., 2017). Narrow-to-broadband conversions remain a challenge in this regard and commonly used
117 conversions are typically designed for use with Landsat-5 or 7, rather than Landsat-8 or Sentinel-2, which increases the
118 uncertainties inherently associated with any narrow-to-broadband conversion (Gardner et al, 2010; Naegeli et al., 2017).

119 In addition, studies assessing the potential effects of anisotropy on satellite-derived surface reflectance data are sparse
120 and the magnitude of associated uncertainties is hard to quantify (Naegeli et al., 2015 & 2017).

121 Naegeli et al. (2019) quantify trends in bare ice albedo for 39 Swiss glaciers using Landsat surface reflectance data
122 products for a 17-year period. While they do not find a clear, wide spread darkening trend of bare ice surfaces
123 throughout the entirety of their data set, they note significant negative trends at the local level, most notably for certain
124 terminus areas. A detailed comparison of different albedo products derived from airborne imaging spectroscopy (APEX)
125 and Landsat and Sentinel data by Naegeli et al. (2017) further highlights the gap between albedo variability on the
126 ground and its representation in remote sensing data of varying resolution. A recent study by Di Mauro et al. (2020)
127 uses in situ HCFR data and DNA analysis to show that ice algae affect albedo on a Swiss glacier.
128
129 Despite the growing body of work on this topic (see Table 1), reflectance properties – spectral as well as broadband,
130 local as well as regional, short time as well as seasonal - remain understudied compared to other parameters routinely
131 recorded at Jamtalferner and other long-term glaciological monitoring sites. However, surface changes and associated
132 changes of the spectral characteristics in the ablation area (e.g. due to debris cover, supraglacial meltwater, deposition of
133 impurities) are expected to play a significant role in determining the future development of these glaciers. Incorporating
134 relevant parameters into monitoring efforts is highly desirable. The accuracy of direct measurements of mass balance
135 depends on the representation of all surface types in the stake network, and the correct attribution of unmeasured areas
136 to measured stake ablation. Accordingly, a better understanding of how surface types differ in terms of their reflective
137 properties is required to maintain the stake network on a rapidly changing glacier. To this end, it is important to
138 understand whether satellite-derived data can provide a basis for defining surface classes to be covered by stakes, or
139 whether it does not allow for the retrieval of the full bandwidth of reflectance variability relevant to the ice melt rate. In
140 addition, delineating the temporal variability of reflectance properties is relevant to degree day modelling, as a changing
141 albedo would alter parameters in the model.
142
143 Table 1: Measurements of bare ice reflectance properties on mountain glaciers: Overview.

| Glacier | Albedo type | Temporal resolution | Spatial resolution | Reference |
| --- | --- | --- | --- | --- |
| Hintereisferner, AT | Total | Multiple days | Multiple points on different surface types | Dirmhirn and Trojer, 1955. |
| Hintereisferner, AT | Total | Multiple times on one day | 2 points | Jaffé, 1960. |
| Northern China (glacier not specified) | Spectral | Not specified | Different surfaces | Zeng et al., 1984. |
| Forbindels, Greenland | Spectral | One measurement campaign | Regular grid of points around multiple study sites | Hall et al., 1990. |
| Hintereisferner, AT | Spectral | 7 days during ablation season | Points along a profile | Van de Wal et al., 1992. |
| Austre Brøggerbreen, Midre Lovénbreen, Svalbard | Spectral, total shortwave | Multiple days during ablation season | 1 point | Winther, 1993. |
| Morteratsch, CH | Narrow band (Landsat TM bands 2 and 4) | One measurement campaign | Multiple points | Greuell and de Wildt, 1999. |
| Haut Glacier d'Arolla, CH | Total | One measurement campaign | Multiple points | Knap et al., 1999. |
| Hintereisferner, AT | Spectral | One measurement campaign | Multiple points | Hendriksa et al., 2003 |
| Morteratsch, CH | Total | Continuous AWS measurements | Multiple AWS locations | Klok et al., 2003 |
| Chhota Shigri, Mera Glaciers, Nepal | Total shortwave | Continuous AWS measurements | AWS location | Brun et al., 2015. |
| Forni Glacier, IT | Total | Multiple measurements during multiple years | Multiple points | Azzoni et al., 2016. |

3

| Glacier de la Plaine Morte, CH | Spectral | One measurement campaign | Multiple points | Naegeli et al., 2015. |
|---|---|---|---|---|
| Findelen, CH | Total | Continuous AWS measurements | AWS location | Naegeli et al., 2017. |
| Morteratsch, CH | Spectral | One measurement campaign | Multiple points | Di Mauro et al., 2017; Di Mauro et al, 2020 |
| Greenland ice sheet | Total | Continuous AWS measurements | Multiple AWS locations | van As et al., 2017; Box et al., 2013 |
| De Geerfonna and Elfenbeinbreen, Svalbard | Total | Continuous AWS measurements | 1 AWS on each glacier | Möller and Möller, 2017 |
| Jamtal, AT | Spectral | One measurement campaign | Multiple points | This study |

144

## 2. Data, Methods, and Study Site

### 2.1. Study site – glaciological background

Jamtalferner was chosen for this study as it has the smallest end-of-season snow cover amongst the glaciers with long term mass balance monitoring in Austria. Jamtalferner is located in the Silvretta mountain range, which intersects the border between Austria and Switzerland. Jamtalferner is the largest glacier on the Austrian side of Silvretta (Fig. 1, size in 1970: 4.115km², size in 2015: 2.818km²). The history of scientific research at the site goes back as far as 1892, when length change measurements were first carried out, and a wealth of cartographic, geodetic, and glaciological data are available (Fischer et al., 2019). Orthophotos and cartographic analysis show that debris cover at the glacier terminus and in the lower elevation zones has increased (debris covered percentage of total area: 1.7% in 1970, 24.1% in 2015), while firn cover is decreasing (firn covered area in 1970: 75%, in 2015: 13%, mean accumulation area ratio (AAR) 1990/91-99/00: 0.35, mean AAR 2010-2017/18: 0.12, Fischer et al., 2016).

Mass balance measurements via the direct glaciological method began in 1988/1989. In recent years, increasing mass loss was recorded across all elevation zones (Fischer et al., 2016). The lowest elevation zones are dominant in terms of total ablation and thus net balance. Melt in the lowest altitudes has been increasing during the last two decades of negative mass balances and the variability of surface albedo at and near the glacier terminus affects melt over the full duration of the ablation season.
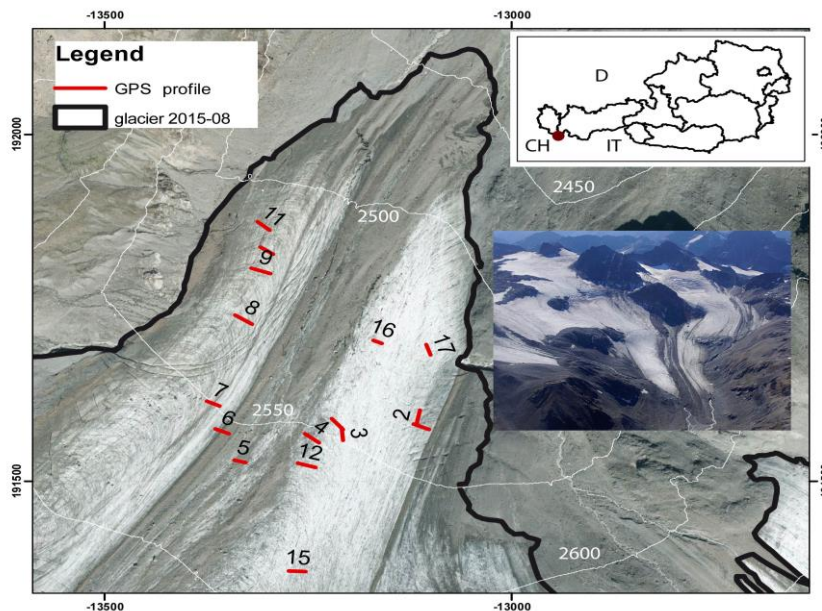


Figure 1: Tongue of Jamtalferner glacier (Orthophoto, August 2015, Source: Tyrolean Government/ TIRIS) with profile lines of spectroradiometer measurements indicated in red. Insert: Aerial photograph of Jamtalferner, 20.09.2018 (Photo: Andrea Fischer).

### 2.2 In situ measurements of spectral reflectance

The field campaign was carried out on September 4th, 2019. This date was selected for two reasons: Favourable weather conditions and temporal proximity to overpasses of both Sentinel-2 (on the same day) and Landsat-8 (on September 3rd). With a large area of high pressure over western and central Europe, the weather at the study site was sunny and dry on throughout Sept. 3rd and 4th. Using an ASD Field Spec Handheld 2 spectroradiometer (ASD Inc., 2010), a total of 246 reflectance spectra (HCFR) was collected, with 12 spectra measured at point locations and 234 spectra measured along 16 profile lines. Profiles were measured along a 20m measuring tape in such a way that individual spectra were gathered at equal intervals, with 14 profile lines containing 11 spectra spaced at 2 m. 2 profiles contain 40 spectra – these were also gathered at equal intervals but with a higher resolution. Measurements began at 08:28 GMT (10:28 local time) and ended at 13:43 GMT. The coordinates of the start and end points of each profile line, as well as any spectra

5

184 measured outside of the lines, were recorded with a Garmin etrex VISTA HCx, a standard handheld GPS device, which
185 also recorded the time of day. The horizontal accuracy of the GPS coordinates is better than 3 m as per the internal
186 accuracy assessment of the GPS device. The timestamps of the GPS points for the start and end points of the profiles
187 were used to compute solar elevation and azimuth. For each profile, the mean solar elevation and azimuth between the
188 respective start and end points is given in Table 2. Measurements were taken 35 cm above ground from nadir with a
189 bare fibre optic cable without additional fore-optics. Test measurements in the field showed high consistency between
190 multiple measurements at the same point, so that we chose to use single measurements at each location rather than
191 average over multiple measurements. The instrument was handheld and not mounted on a stand to minimize shading.
192 This measurement set up is similar to that of previous studies (Naegeli, 2015; Di Mauro et al., 2017) and yields a
193 circular field of view (FOV) with a radius of approximately 7.8 cm for flat ground. The instrument operates between
194 325 and 1075 nm with an accuracy of $\pm 1$ nm and a resolution of <3 nm at 700 nm. We used a feature of the instrument
195 that allows the user to save the white reference measurement to the RAM of the built-in computer. HCFR is computed
196 for subsequent target reflectance measurements based on the saved reference. This is saved to the output file,
197 eliminating the need to calibrate the target measurements to the white reference in post-processing. A new SRT-- 99-020
198 Spectralon (serial number 99AA08-0918-1593) manufactured by Lab Sphere was used for the measurement of the
199 white reference. The ASD data files were imported into a python script for further analysis using the Python module
200 SpecDal (Lee, 2017) to read the ASD format. Further data analysis was carried out using numerous other Python (Van
201 Rossum and Drake., 2009) packages, mainly NumPy (van der Walt et al., 2011), pandas (McKinney, 2010), Matplotlib
202 (Hunter, 2007), Rasterio (Gillies et al., 2013), GeoPandas (GeoPandas developers, 2019), rasterstats (Perry, 2015), and
203 PyEphem (Rhodes, 2020).

204
205
206 **2.3 Satellite data**
207
208 We compare the in situ measurements with surface reflectance products derived from a Landsat-8 Operational Land
209 Imager (OLI) scene acquired on September 3rd, 2019 (10:10 GMT), the day before the field campaign, and a Sentinel
210 2A scene acquired on September 4th (10:20 GMT), the same day as the field campaign. Both scenes are cloud free over
211 the study area (Figure 2). Details on the atmospheric correction algorithm used to generate the Landsat-8 OLI level-2
212 surface reflectance data product from top of atmosphere (TOA) reflectance can be found in Vermote et al. (2016) and in
213 the product guide of the algorithm used to derive surface reflectance (USGS, 2020). Details on the equivalent Sentinel-2
214 product – the Level-2A bottom of atmosphere reflectance – are given in Main-Knorn et al. (2017) and Richter and
215 Schläpfer (2011). For the sake of readability, we refer to the Landsat-8 OLI level-2 surface reflectance as "Landsat"
216 data in the following, and to the Sentinel-2 level-2A surface reflectance as "Sentinel" data. The Landsat and Sentinel
217 surface reflectance raster data used in this study were acquired using Google Earth Engine (Gorelick et al., 2017).
218
219 The wavelength range of the spectroradiometric measurements carried out on the ground overlaps with bands 1-5 of the
220 Landsat data and bands 1-9 and 8A of the Sentinel data, respectively. Only spectral ranges covered by these bands are
221 considered for this study. The wavelengths and resolution of the individual bands, as well as the relevant viewing and
222 solar angles are given in Table 3. For each ground measurement point, band values were extracted from the satellite
223 scenes at the overlaying pixel.
224
225 In order to compare the satellite values with ground data, we compute mean values for the subsets of the spectral
226 reflectance curves measured on the ground that correspond to the Landsat and Sentinel bands, respectively. Data are
227 then grouped into profile lines and/or different bands, the Pearson correlation is computed for ground- and
228 corresponding satellite data, and further comparisons are carried out using standard statistical metrics.
229
230 To assess the influence of the spatial resolution of the satellite data on results, band 3 imagery was resampled (cubic
231 interpolation) from the original 10 m resolution to 30 m and 60 m for Sentinel and from 30 m to 60 m for Landsat,
232 respectively. To account for the potential effects of the uncertainty in the GPS coordinates, we created a circular buffer
233 with a radius of 3m around each in situ measurement point. For each buffer, the corresponding satellite value is
234 computed as the median of the values of all pixels the buffer overlaps with.
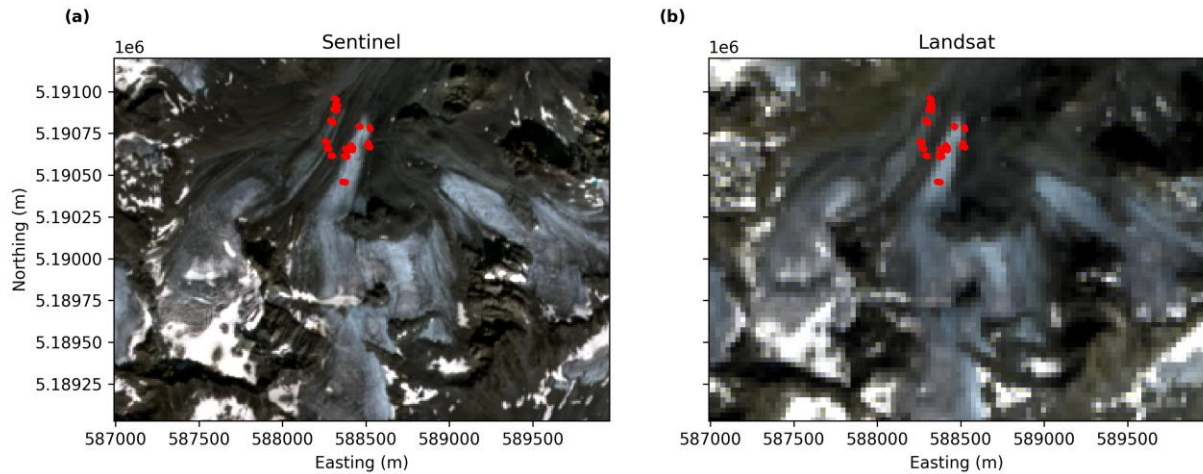
Figure 2: Jamtalferner as seen in the Sentinel (a) and Landsat (b) scenes used in this study. The images shown here are composites of bands 2, 3, and 4 of each satellite's L2A surface reflectance product displayed at a resolution of 10 (Sentinel) and 30 (Landsat) m/pixel, respectively. Profiles where reflectance spectra were collected are marked in red. Coordinate reference system: EPSG: 32632.

## 3. Results

### 3.1 Surface measurements

The in situ measurements exhibit extreme differences in HCFR depending on the characteristics of the surface. Figure 3 shows the spectra grouped into profiles, with the mean spectral HCFR highlighted for each profile. P3 is the "brightest" profile, with the highest maximum (up to 0.7) and minimum (up to 0.2) values of all profiles. Profiles 2, 11, and 14 are the darkest profiles and all of their respective spectral reflectance remain below 0.2 at all measured wavelengths. Figure 3 also shows the ice surface along profile lines 3 (brightest) and 11 (darkest) for a visual comparison. In P3, the surface is mainly comprised of clean, dry ice. In P11, the ice surface is wet and impurities (rocks, fine grained debris) are present. The profile line crosses several small melt water channels with running water.

7
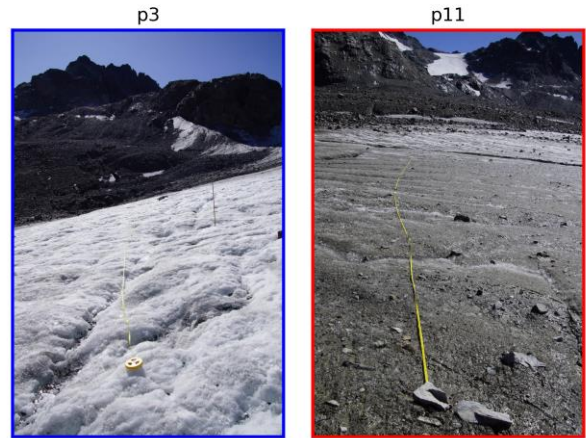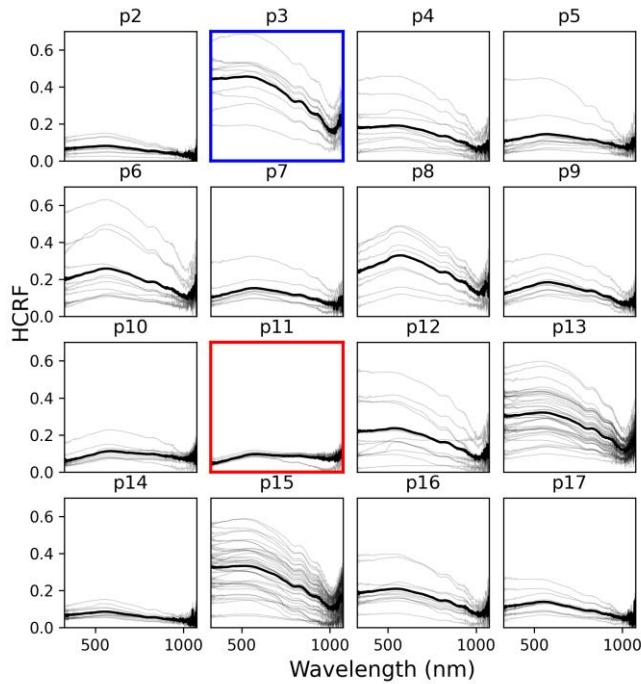
Figure 3: Each subplot on the left shows the spectra along a profile line. The bold black lines highlight the mean spectral reflectance (HCRF) in each profile. Fotos of the ice surface along p3 and p11 are shown on the right for visual context. Fotos were taken at the time of the respective measurements by A. Fischer.

Table 2 contains a qualitative description of the ice surface along each profile line, the length of the line, the number of spectra per line, and the number of Landsat and Sentinel band 3 pixels that each line crosses, as well as the mean solar elevation and azimuth angles for the profile. The maximum number of pixels per line is 5 for Sentinel and 3 for Landsat, respectively. All lines cross at least 2 pixels for Sentinel, while 3 lines fall into a single Landsat pixel. See Fig. 1 for the location of each profile on the glacier.

Table 2: Description of the surface characteristics along each profile line, as well as number of spectra collected along the line and number of pixels intersected by the line in band 3 of the Sentinel and Landsat scenes, respectively.

| Profile Nr. | Qualitative description | Mean solar elevation, azimuth in degrees | Spectra | Sentinel B3 pixels | Landsat B3 pixels |
|---|---|---|---|---|---|
| P2 | Relatively smooth, uniform ice surface, slightly wet. | 24.69, 106.70 | 11 | 3 | 2 |
| P3 | Mostly dry surface, clean cryoconite. | 26.43, 108.92 | 11 | 4 | 1 |
| P4 | Mostly dry ice surface, some dirt, some rocks/debris on ice surface where profile approaches moraine. | 28.64, 111.87 | 11 | 4 | 2 |
| P5 | Significant debris cover along profile. Where ice is exposed, ice surface is wet. Profile crosses meltwater channels with running water. | 31.34, 115.72 | 11 | 3 | 1 |
| P6 | Wet ice surface with dust/dirt transitions to cleaner, brighter ice. | 34.45, 120.61 | 11 | 4 | 1 |
| P7 | Grey-ish ice surface with meltwater channels and fine-grained debris/small rocks. | 36.20, 123.57 | 11 | 2 | 2 |
| P8 | Similar to P7, fewer rocks. | 38.05, 126.99 | 11 | 4 | 2 |
| P9 | Wet ice surface with mixture of relatively clean cryoconite and more dusty areas. | 39.40, 129.68 | 11 | 3 | 2 |
| P10 | Wet ice surface with several small melt water channels. Mostly dirty, grey ice. | 40.71, 132.51 | 11 | 3 | 2 |
| P11 | Wet ice surface with several small meltwater channels. Very dirty ice with scattered small rocks. | 42.08, 135.75 | 11 | 4 | 2 |

8

| **P12** | Relatively clean, bright ice interspersed with larger meltwater ponds/channels, which contain dirt and small rocks. | 47.61, 153.83 | 11 | 4 | 3 |
|---|---|---|---|---|---|
| **P13** | Clean cryoconite with some darker patches. | 48.63, 159.14 | 40 | 5 | 2 |
| **P14** | Wet ice surface with fine grained dirt in relatively uniform cryoconite. | 49.80, 168.30 | 11 | 4 | 2 |
| **P15** | Uneven ice surface, mostly clean, dry ice. | 50.30, 179.29 | 40 | 3 | 2 |
| **P16** | Mixture of wet and dry ice surface and fine-grained dirt. | 49.43, 194.99 | 11 | 3 | 2 |
| **P17** | Mostly wet ice surface, fine grained dirt with some cleaner patches. | 48.33, 202.34 | 11 | 2 | 2 |

The spectral reflectance curves of the individual spectra as well as of the profile lines indicate high spatial variation of surface types and associated reflective properties. The spectral signatures of the individual spectra can roughly be grouped into dry ice, wet ice, and dirt/rocks. (We use the word "dirt" to describe all types of mineral or organic materials and fine-grained debris that may collect on the glacier surface.) However, transitions between these types are gradational and in practice these categories cannot always be clearly separated - both dry and wet ice might be clean or dirty, dirt might be wet or dry.

The reflectance curves for clean ice exhibit the typical shape frequently found in literature (Zeng et al., 1984), with highest reflectance values (up to 0.69) in the lower third of our wavelength range and declining values for wavelengths greater than approximately 580 nm. The spectral reflectance curves of wet ice surfaces follow roughly the same shape as for dry ice but are strongly dampened in amplitude with reflectance values typically not exceeding 0.2. In contrast, the reflectance curve of dirty surfaces remains at uniformly low values throughout our wavelength range in some cases and exhibits an increase between 325 and approximately 550 nm before flattening out in other cases. Reflectance values have similar magnitudes as for wet ice. Example reflectance curves of these surface types are given in Fig. 4.
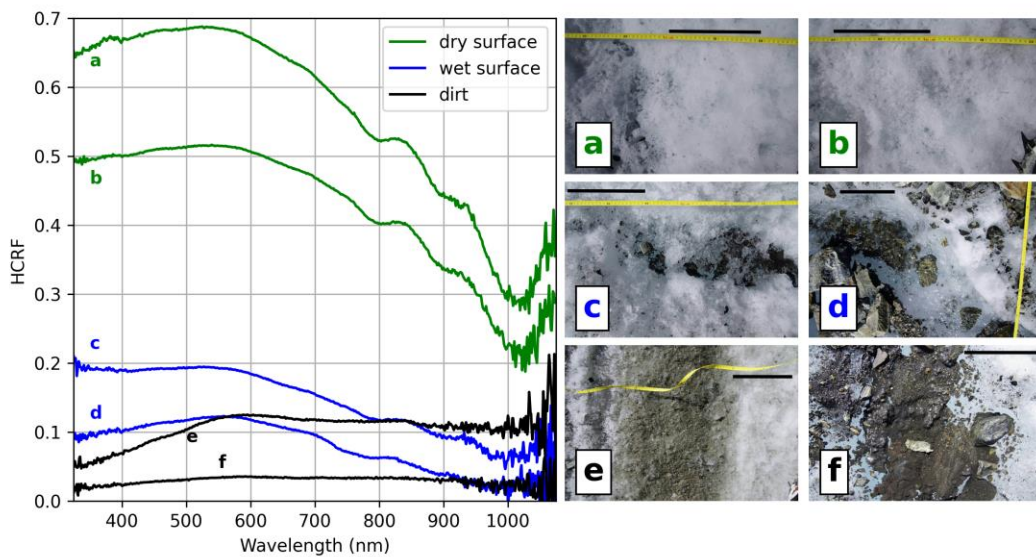


Figure 4: Spectra of different kinds of ice surface types encountered in the ablation zone of Jamtalferner. The photos on the right show the ice surface at the sampling sites of the respective spectra. The black bar in each photo represents approximately 20 cm, to provide a sense of scale. The spectra shown in this figure are part of the following profile lines: a, b, c – p3; d – p4; e – p6; f – p12.

### 3.2 Comparison with satellite data

Figure 5 shows all measured spectral reflectance curves, as well as the Sentinel and Landsat values in the bands that overlap the wavelength range of the ground measurements. Reflectance values were extracted from the satellite imagery at the coordinates of each sampling point and overlayed onto the plots of the in situ spectra as coloured bars. Naturally, neither satellite captures the full range of reflectance values measured on the ground. In all overlapping bands of

9

299 Sentinel and Landsat, the Sentinel values are higher, in the sense that the maximum values of the Sentinel data are
300 closer to the maximum values measured on the ground, while the minimum Landsat data are closer to the minimum
301 values measured on the ground.
302
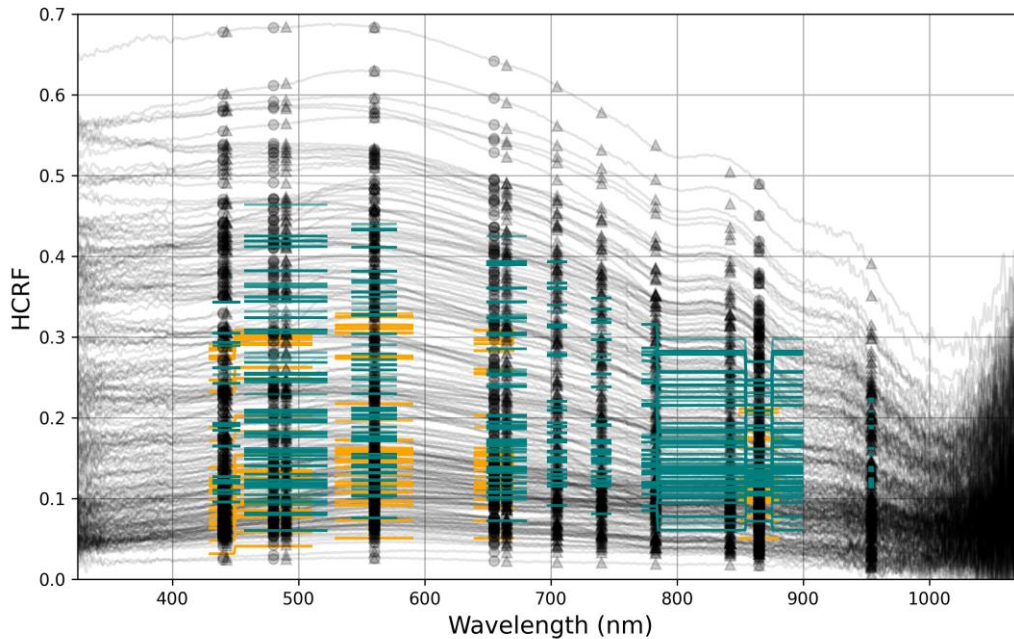


303
304
305 Figure 5: The spectra measured in situ are plotted in black. Black circles indicate the central wavelengths of the Landsat
306 bands, black triangles those of the Sentinel bands (see Table 3). Orange and blue lines represent the wavelength range of
307 the respective Landsat and Sentinel bands along the horizontal axis and the satellite derived reflectance at the sampling
308 points of each spectrum on the vertical axis.
309
310 Comparing the mean of the HCRF spectra measured on the ground for each satellite band with the associated satellite
311 values yields a Pearson correlation coefficient ranging from 0.53 (band 5) to 0.62 (band 1) for the Landsat bands and
312 0.3 (band 9) to 0.65 (band 2) for Sentinel. Table 3 lists the correlation coefficients, as well as the wavelength range and
313 resolution of each band. The two lower resolution Sentinel bands (band 1, band 9 – 60m resolution) have notably lower
314 correlation coefficients than the higher resolution bands. The Sentinel and Landsat data at the in situ measurement
315 points are strongly correlated with each other in the bands where both satellites overlap, with r=0.69 in band 1 and r>0.8
316 for bands 2, 3, 4, and 5.
317
318 For a visual comparison of the location of the profile lines and the range of measured values in the profiles in relation to
319 the satellite pixel boundaries and pixel band values, see Fig. 6 for Sentinel (band 3 selected as an example) and
320 supplementary material for an analogous figure of the Landsat data.
321
322 Table 3: Band names and respective wavelength range and resolution for Landsat and Sentinel as used in this study.
323 Pearson correlation given for mean band values of ground-measurements and associated satellite data. For Landsat, the
324 solar zenith and azimuth angles given in the surface reflectance image are listed. The view zenith angle is hardcoded to
325 0 in the Land Surface Reflectance Code (LaSRC_1.3.0) for the Landsat surface reflectance product, as per the LaSRC
326 documentation (USGS, 2020). For Sentinel, the incidence angles refer to the mean viewing zenith and azimuth angles
327 for each band. The solar angles are the averages for all bands.
328

| Band | Landsat | Sensing time: 2019-09-03 10:10 GMT | | | | | |
|---|---|---|---|---|---|---|---|
| Band | Range (nm) | Resolution (m) | Pearson Corr. | View zenith angle | View azimuth angle | Solar zenith angle | Solar azimuth angle |

10

| | | | | Mean incidence zenith angle | Mean incidence azimuth angle | Mean solar zenith angle | Mean solar azimuth angle |
|---|---|---|---|---|---|---|---|
| 1 (Coastal/Aerosol) | 430-450 | 30 | 0.62 | 0 | - | 42.63 | 153.57 |
| 2 (Blue) | 450-510 | 30 | 0.61 | | | | |
| 3 (Green) | 530-590 | 30 | 0.58 | | | | |
| 4 (Red) | 640-670 | 30 | 0.57 | | | | |
| 5 (NIR) | 850-880 | 30 | 0.53 | | | | |
| | **Sentinel** | Sensing time:2019-09-04 10:20 GMT | | **Mean incidence zenith angle** | **Mean incidence azimuth angle** | **Mean solar zenith angle** | **Mean solar azimuth angle** |
| 1 (Coastal/Aerosol) | 433-453 | 60 | 0.46 | 3.13 | 193.02 | 40.83 | 159.93 |
| 2 (Blue) | 457.5-522.5 | 10 | 0.65 | 2.48 | 198.51 | | |
| 3 (Green) | 542.5-577.5 | 10 | 0.63 | 2.59 | 196.22 | | |
| 4 (Red) | 650-680 | 10 | 0.61 | 2.72 | 194.92 | | |
| 5 (Vegetation Red Edge) | 697.5-712.5 | 20 | 0.57 | 2.79 | 194.43 | | |
| 6 (Vegetation Red Edge) | 732.5-747.5 | 20 | 0.56 | 2.87 | 193.84 | | |
| 7 (Vegetation Red Edge) | 773-793 | 20 | 0.55 | 2.95 | 193.53 | | |
| 8 (NIR) | 784.5-899.5 | 10 | 0.56 | 2.54 | 197.22 | | |
| 8A (NIR narrow band) | 855-875 | 20 | 0.53 | 3.04 | 193.30 | | |
| 9 (Water vapour) | 953-955 | 60 | 0.3 | 3.22 | 192.89 | | |

329
330
331
332
333

11
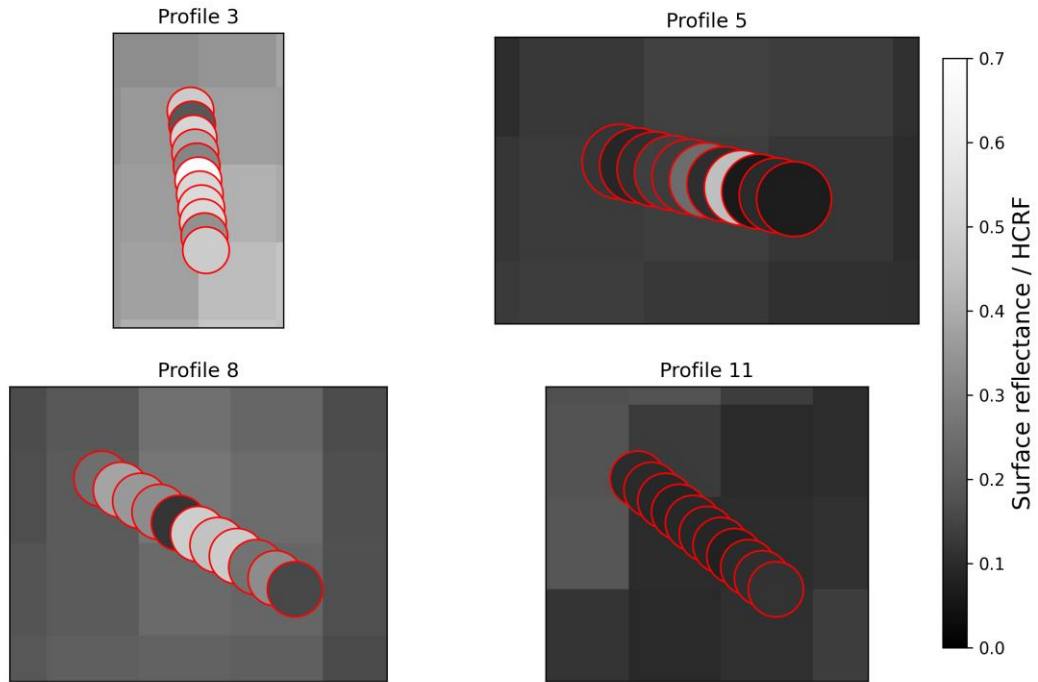
Figure 6: The spectra comprising the profile lines are plotted over the corresponding satellite pixels for selected profiles. The colour bar is the same for the background raster and the circles indicating the sampling sites of the spectra and represents the Sentinel band 3 pixel value and the mean reflectance in the Sentinel band 3 wavelength range of each spectrum, respectively. The pixel size of the raster is 10m². The GPS coordinates of the sampling sites are centred in the circles. The circle radius is set to 3m to represent the horizontal uncertainty of the GPS points.

The spread of in situ HCRF values per profile is generally lower for profiles that are darker overall, and greater for brighter profiles, although not in all cases (Fig. 3, Fig. 7). In the Sentinel band 3 wavelength range, profile 3 is brightest with a median reflectance of 0.48 and spread of 0.49. Profile 6 (median in Sentinel band 3 range: 0.21) has the largest spread of HCRF (0.52). Broadly speaking, profiles with a high median HCRF tend to include individual measurement points that are both very bright and very dark, while darker profiles are more uniformly dark. Profile 6 in particular transitions between surface types and contains wet/dirty spectra as well as dry ice spectra (see Table 2). Figure 7 shows boxplots of the ground measurements (band 3 mean) for all profiles to exemplify this and indicates where the Landsat and Sentinel values fall compared to the spread of values in each profile.
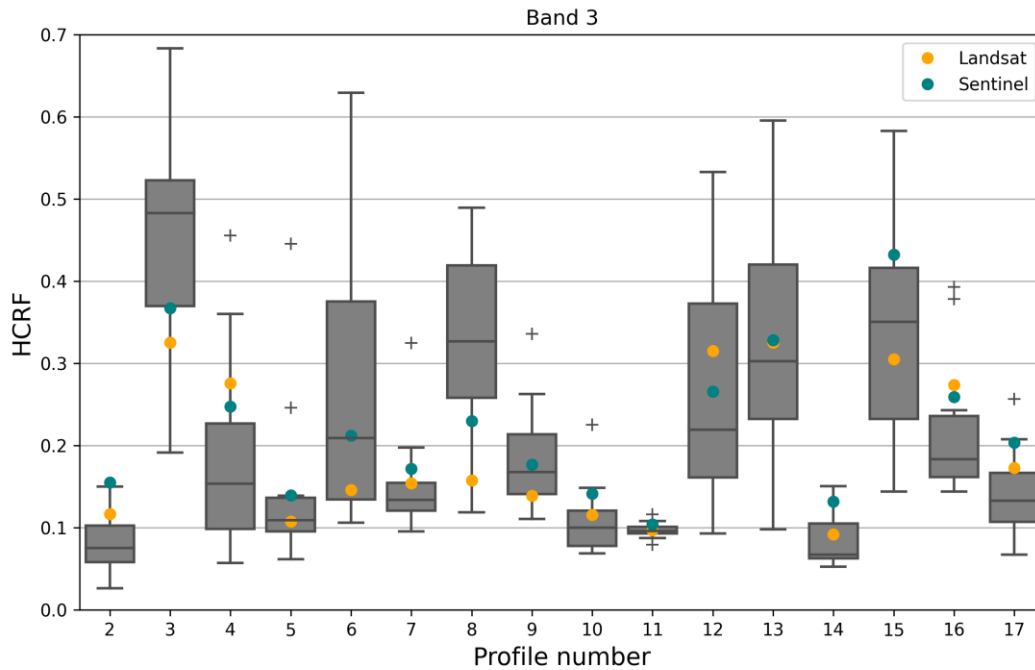
Figure 7: Spread of the Sentinel band 3 (wavelength range: 542.5-577.5 nm) mean values of the measured spectra, grouped by profile. Orange and blue circles show corresponding mean pixel values of data extracted from Landsat and Sentinel pixels at the sampling sites of the spectra, respectively. The boxes represent the first and third quartile. The whiskers represent 1.5x the interquartile range, the + symbols are outliers.

When binning in situ measurements by the associated satellite value/pixel and taking the median or mean of the binned values, the difference between the median/mean in situ value and the satellite value tends to decrease with increasing number of in situ measurements mapped to unique satellite values. This is to be expected, as each satellite value represents an integration of the emission characteristics over the area contained in the pixel. However, for our data, this relationship is not obviously linear and differs between Sentinel and Landsat, as well as between different bands (Figure 8).

Comparing in situ and satellite values for individual in situ measurement points, it is apparent that both satellites tend to overestimate the reflectance values of dark ground surfaces, and underestimate the reflectance of bright surfaces, in all bands (Figure 9). The shift from over- to underestimation appears linear and has a similar increase rate in all bands. The zero crossings of the regression lines, i.e. the ground reflectance values for which ground measurements and satellite values match, fall between 0.15 (band 5) and 0.21 (band 1) for Landsat and 0.17 (band 9) and 0.27 (band 3) for Sentinel.

Figure 10 shows histograms of the mean reflectance in band 3 of Landsat and Sentinel, respectively, compared with associated in situ values, as well as density plots of the satellite derived surface reflectance over all pixels in the study area. The mean is highest in the in situ measurements and lowest in Landsat images. Both Sentinel and Landsat fail to capture HCRF values below 0.05 and above 0.45. A second peak in frequency evident from the in situ measurements at a reflectance of 0.4 is not represented in the remote sensing data.
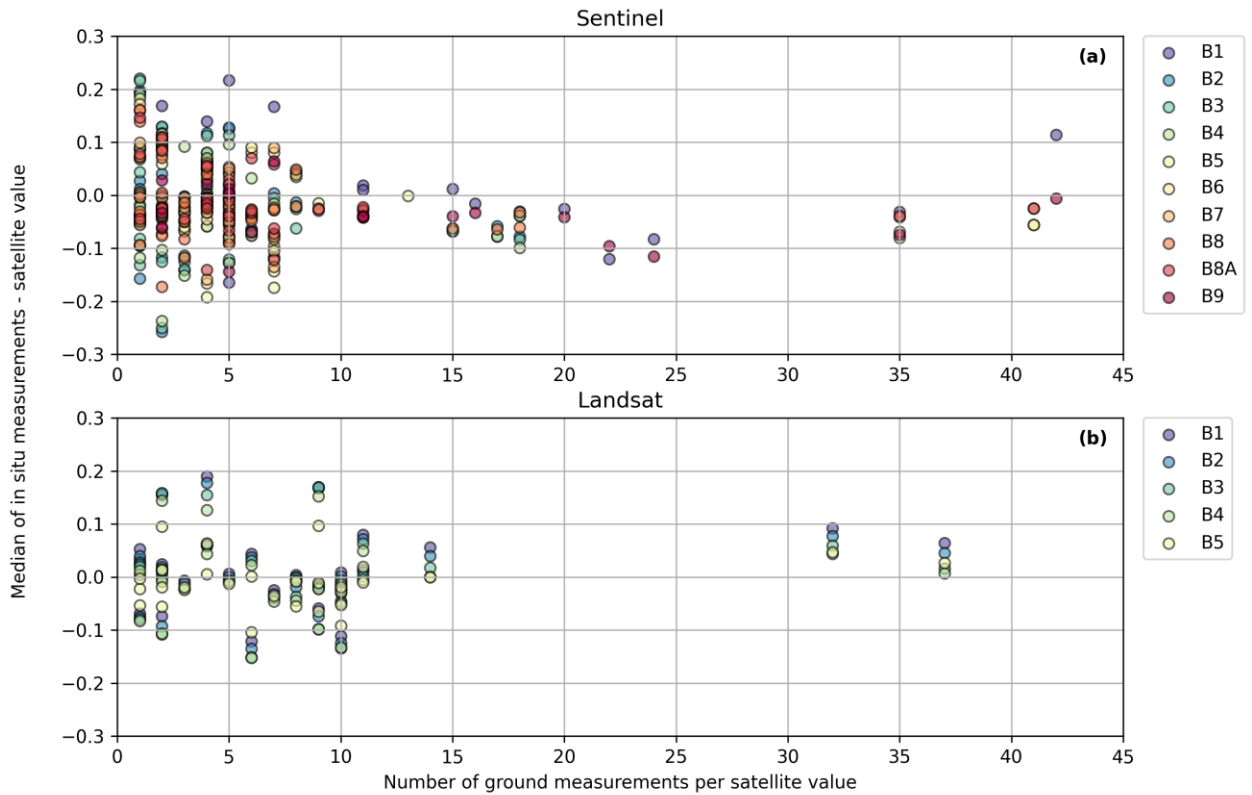
13

Figure 8: The number of ground measurements per unique satellite value (x-axis) is plotted against the difference between the median of these ground measurements in the respective wavelength band and the corresponding satellite value (y-axis). i.e. values that are positive in the vertical axis represent cases where ground reflectance is higher than satellite derived reflectance, whereas negative values represent the opposite. Different colours represent the different satellite bands, as indicated by the legend next to the plots.

14
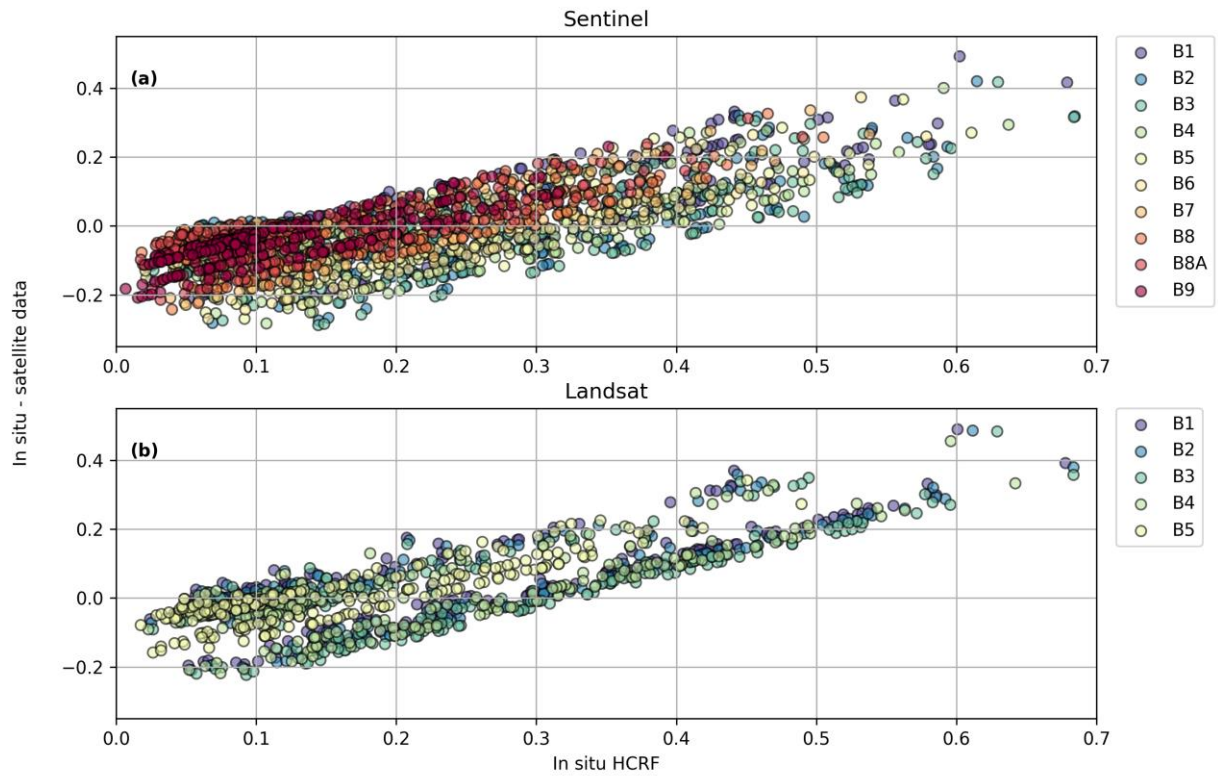
384
385
386 Figure 9: Same data as in Fig. 8, but showing individual sampling points without grouping by common satellite pixels.
387
388
389
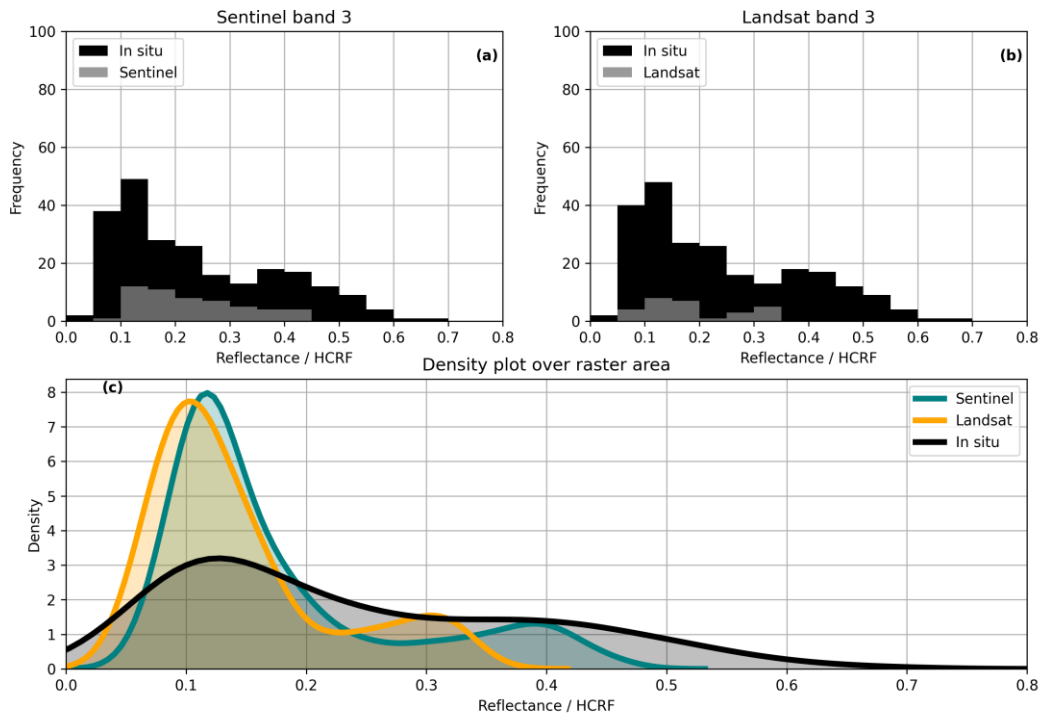


390

391
392 Figure 10: The histograms in the top panels (a, b) show the frequency of occurrence of the band 3 mean values of the
393 ground measurements per reflectance bin. Bin width: 0.05. Overlaid in grey are the histograms of the corresponding
394 satellite pixel values. The bottom panel (c) shows density plots of the Sentinel and Landsat band 3 surface reflectance
395 rasters over the study area (smallest possible rectangle containing all ground measurements), with the density of the in
396 situ HCRF for comparison.
397
398 To conclude the results, a note on the sensitivity of data and results to the spatial resolution of the satellite data and the
399 accuracy of the geolocation of the in situ data: To assess the possible effects of the GPS accuracy or lack thereof, we
400 compare the differences between in situ and satellite values presented previously to the differences that result when a
401 buffer corresponding to the GPS uncertainty is created around each in situ measurement point. For the Sentinel data in
402 the original 10 m resolution of band 3, the maximum number of pixels that any buffer touches is 4, the mean is 2.6, and
403 most buffered in situ measurement points overlap with 2 pixels. For the 30 m Landsat data in band 3, the maximum
404 number of pixels touched is also 4 while the mean is 1.5 and most in situ points are fully within only one pixel. Table 4
405 gives the standard deviation of differences between the in situ HCFR and the satellite data in different resolutions,
406 grouped by the number pixels the buffered measurement points overlap with, to show how variability of results shifts
407 depending on the buffer and the raster resolution. Changes caused by introducing the buffer are small in all groups. As
408 expected, standard deviation increases with decreasing resolution of the satellite pixels due to the loss of detail in the
409 satellite data. Figure 11 gives an overview of the ungrouped dataset with and without the buffer and at different raster
410 resolutions.
411
412 Table 4: Comparison of in situ and satellite data by the standard deviation (SD) of the difference between in situ HCFR
413 and satellite surface reflectance. Values are grouped by number of pixels that buffered in situ measurements overlap.

| | Sentinel | | | | | Landsat | | | |
|---|---|---|---|---|---|---|---|---|---|
| Nr. of overlapping pixels | Nr. of points | SD, no buffer, 10m | SD, buffer, 10m | SD, buffer, 30m | SD, buffer, 60m | Nr. of points | SD, no buffer, 30m | SD, buffer, 30m | SD, buffer, 60m |
| 1 | 25 | 0.098 | 0.098 | 0.108 | 0.129 | 134 | 0.129 | 0.129 | 0.134 |
| 2 | 124 | 0.119 | 0.118 | 0.120 | 0.124 | 94 | 0.106 | 0.107 | 0.103 |
| 3 | 9 | 0.057 | 0.065 | 0.069 | 0.099 | 1 | - | - | - |
| 4 | 76 | 0.122 | 0.121 | 0.127 | 0.136 | 5 | 0.082 | 0.074 | 0.083 |

414
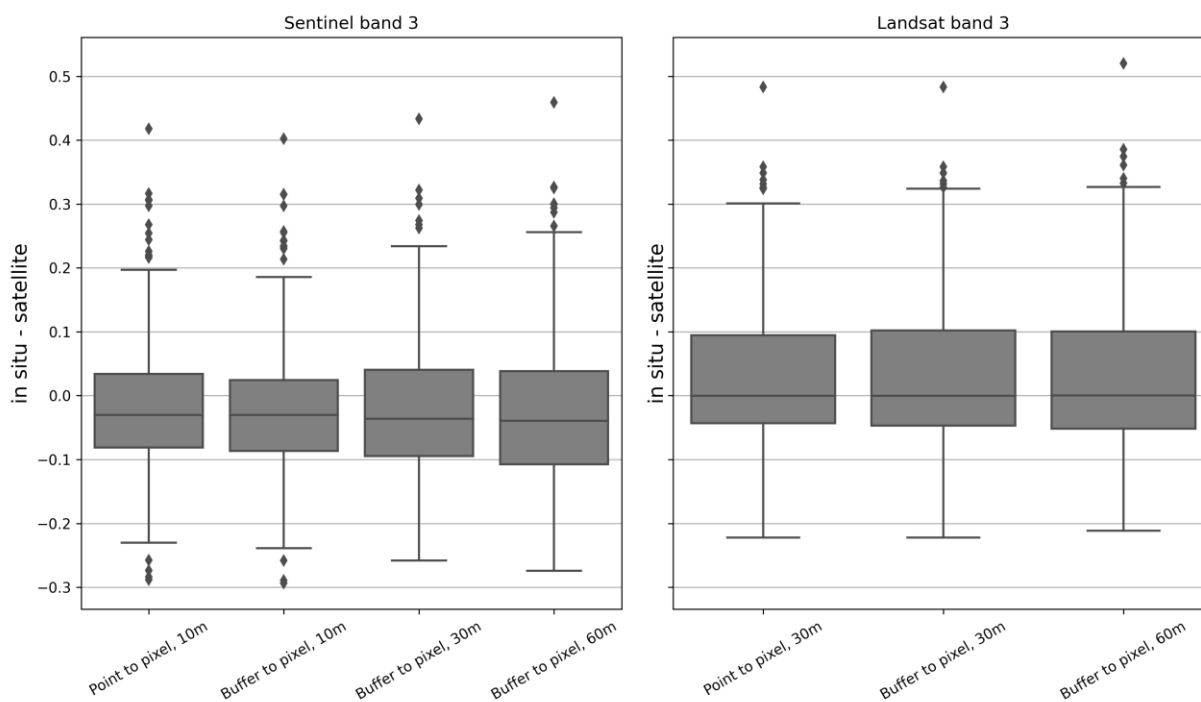
Figure 11: For the respective Sentinel and Landsat band 3 wavelength range, the difference between the in situ HCRF and satellite surface reflectance product is on the vertical axis. Point to pixel refers to the data as presented in previous figures. Buffer to pixel refers to data generated using a buffer around the in situ measurement points to account for GPS accuracy. For Sentinel, the original 10m resolution data was resampled to 30 and 60m. For Landsat, the original 30m resolution data was resampled to 60m.

## 4. Discussion

There are a number of complexities associated both with measuring reflectance properties on the ground and with any comparison between different products and data sets. Perhaps more than anything else, our results highlight the need for further in situ measurements and targeted data collection campaigns designed specifically to address some of the uncertainties detailed in the following.

### 4.1. Reflectance anisotropy and changing solar and atmospheric conditions

Ice is an anisotropic material and previous studies have shown that for glacier surfaces, anisotropy increases with decreasing albedo and depends on wavelength and solar zenith angle (Greuell and de Wildt, 1999; Klok et al., 2003; Naegeli et al., 2015). In order to truly quantify the effects of anisotropy in in situ spectroradiometric measurements, the bidirectional reflectance distribution function (BRDF) must be obtained – ideally for each measurement point. The BRDF cannot be measured directly but is approximated, e.g. by interpolating between multi-angular spectroradiometer measurements (Naegeli et al., 2015), or with modelling approaches (Malinka et al., 2016). While multi-angular HCRF measurements allow for the estimation of the BRDF, they are intrinsically dependent on the atmospheric conditions (cloud cover) at any given time, as well as on the topography and structure of the surface. Naegeli et al. (2015, 2017) use this approach to develop anisotropy correction factors for different glacier surface types in order to account for the typical underestimation of albedo in observations from nadir in remote sensing data. They find a difference between corrected and uncorrected albedo values of up to 11% for dirty ice in airborne imaging spectroscopy data. Nonetheless, the application of constant correction factors for clustered surface types is a simplification that obscures both the gradational nature of surface classification and the complexity of accounting for the effects of varying surface roughness on effective illumination angles. We consider a quantitative assessment of anisotropy beyond the scope of our study and hope to tackle this issue in detail in future work. We assume that our in situ data as well as the satellite products underestimate the quantities they measure (HCRF and surface reflectance as per the respective documentation of the satellite products) due to the nadir or near-nadir observational angle, in particular for dark surfaces, and that uncertainties caused by anisotropy are likely to be in the range found by Naegeli et al. (2017). The local variability of reflectance properties of glacier ice is comprised of the spectral, as well as spatial and temporal variability of reflectance anisotropy, which require a combination of targeted, continuous measurements and modelling that accounts for the

17

449 surface roughness of different glacier surface types to truly delineate.

450 The weather on September 3 (Landsat overpass) and September 4, 2019, (Sentinel overpass, in situ measurements) was
451 very favourable. There was no cloud cover at the study site during either of the satellite overpasses and for the duration
452 of the field measurements and we consider any changes in atmospheric conditions to be negligible. While the
453 illumination angles naturally change over the course of the day and accordingly changed during the in situ
454 measurements (Table 2), very low solar elevation angles were avoided. In their study on parametrizing BRDFs for
455 glacier ice and Landsat TM, Greuell and de Wildt (1999) show that the spectrally integrated albedo of dark ice changes
456 with the solar zenith angle and is particularly low for low zenith angles. Accordingly, we acknowledge that the changing
457 solar angles are a source of uncertainty in our data and the comparison with the satellite derived reflectances, but we
458 consider this uncertainty relatively small since measurements were carried out within a few hours before and after the
459 satellite overpasses, avoiding very low solar elevation angles. Greuell and de Wildt (1999) also point out that the drop in
460 albedo for low zenith angle is related to the presence of meltwater at later times of day (lower zenith angles), which
461 highlights the difficulty of isolating one variable (zenith angle) in a complex system with multiple variables that change
462 over time (surface processes like meltwater affecting reflectance properties).

463 The Landsat and Sentinel surface reflectance products both incorporate an atmospheric correction applied to TOA
464 reflectance in the generation of the BOA product (Vermote et al., 2016; Main-Knorn et al., 2017). This introduces some
465 uncertainty into the comparison with in situ data since the correction methods differ. Nonetheless, we believe that
466 assessing how in situ data compare to the frequently used surface reflectance products of the Landsat-8 and Sentinel-2
467 suites is a necessary first step in being able to determine whether custom atmospheric corrections would improve results
468 and if such improvements would be large enough to outweigh the added complexity and computational cost. We suggest
469 that the answer to this question depends on the application and the spatial scale of the intended analysis. Again, this is
470 beyond the scope of the presented study and is a point that needs to be specifically addressed in future work. We suggest
471 that case studies at individual, well-studied glaciers can serve as an ideal testing ground for such issues, and will help to
472 determine whether custom atmospheric corrections should be applied and are feasible on a regional or even global scale
473 in satellite-based studies of ablation area reflectance properties.

474 **4.2. Implications of in situ and satellite comparison**

475 The results presented in section 3.1. highlight the large spatial variability of HCRF and different surface types
476 encountered in the ablation area, both of which are in line with findings from other studies (Naegeli et al., 2015, 2017;
477 Di Mauro et al., 2017). Section 3.2., the comparison of the in situ data with satellite values, arguably presents greater
478 challenges in terms of interpretation and implications of the results.

479 In summary, there are three key findings which we believe may be important for further studies and for delineating the
480 relationship between in situ and satellite derived reflectance:

481 • Sentinel surface reflectance values tend to be closer to the higher end of HCFR values measured in situ, while
482 Landsat tends to be closer to the in situ minimum.
483 • The difference between in situ data and satellite data tends to decrease when there are more in situ data points
484 per pixel, but not always and not in a clearly linear way.
485 • The reflectance of dark surfaces tends to be overestimated in the satellite products, while the reflectance of
486 bright surfaces tends to be underestimated.

487 Explaining the above points in full requires targeted investigations specifically addressing the contributing factors and
488 uncertainties, which – with our current data set – we can only provide a qualitative overview of:

489 As mentioned previously, different atmospheric corrections are used for the Sentinel and Landsat surface reflectance
490 products. This may contribute to systematic differences in how surface reflectance is represented under differing
491 lighting conditions and in different spectral ranges. Efforts to harmonize the Landsat and Sentinel surface reflectance
492 data sets have great potential for minimizing this problem for applications where data from both satellites is used
493 (Claverie et al., 2018).

494 Another issue that deserves more detailed attention is the narrow/spectral to broad band conversion required for
495 comparing satellite reflectance in individual bands with the in situ data of the same wavelength range. We intentionally
496 do not compute a shortwave broadband albedo from the satellite band values or the spectral in situ data to avoid
497 introducing a further source of uncertainty. Instead, we limit ourselves to averaging over the band wavelength range in
498 order to keep the comparison as straightforward as possible, but acknowledge that a glacier wide broad band albedo is a

18

499  key parameter for many regional or global modelling applications.

500  The standard atmospherically corrected BOA reflectance products from satellite data are provided without correcting
501  for the BRDF. The BRDF, describing the change of the reflectance with different observation and incidence geometries,
502  can have a significant impact on the satellite-based reflectance as well as on the in situ data, leading to inherent
503  challenges when comparing satellite based BOA reflectance with in situ reflectance measurements (Schaepman-Strub et
504  al., 2006). Correcting Landsat and Sentinel surface reflectance with MODIS or VIIRS BRDF products to produce
505  surface albedo has been shown to be a viable approach in some cases (Shuai et al., 2011; Li et al., 2018), but the coarse
506  resolution of MODIS and VIIRS data is unlikely to capture the small-scale anisotropy effects of different glacier surface
507  types. This would therefore be of limited use for our purposes. Optimizing methods for computing surface albedo from
508  the L2A products, as well as from the in situ HCRF, requires further study and customized solutions accounting for
509  local topographic effects and the spectral characteristics of the surfaces. We assume that for our case uncertainties due
510  to the intrinsic difference between HCRF and satellite derived HDRF are small compared to other sources of
511  uncertainty: The influence of local topography as a source of indirect radiation is not represented in the satellite derived
512  values and the microstructure of the ice surface may locally affect in situ values on a scale that not visible to the
513  satellite, but could be very significant for in situ measurements (e.g. small ice ridges or similar features acting as
514  reflectors and/or scattering light into the FOV of the instrument).

515  Hendricks at al. (2004) state for spectroradiometric measurements at Hintereisferner compared to Landsat ETM+
516  imagery acquired about 2 weeks before the field measurements: "The reflectance of ice seems to be highly variable with
517  both under -and overestimations of up to 76 % and 31 % respectively." This corresponds well with our finding that both
518  under- and overestimation occur frequently for both satellites. The factors mentioned above may partly explain the
519  location of the shift from under- to overestimation (Fig. 9), but –again- targeted measurement campaigns are needed to
520  truly quantify this.

521  The influence of very local backscattering could play a role in the seeming inconsistencies in the dependency of the
522  difference between in situ and satellite data the on number of in situ measurement points per pixel (Fig. 8), but this also
523  ties in with questions regarding the positional accuracy of the in situ measurement points and the satellite data, and the
524  spatial representativity of point measurements for a larger area:

525  Our comparison of in situ and satellite data is based on the assumption that we know where both are located in a
526  common coordinate reference system to a sufficient degree of accuracy. The accuracy of the position of the GPS points
527  at the start and end points of the measurement profiles is approximately 3m. Sentinel-2 orthorectification is based on the
528  PlanetDEM 90 digital evelation model (DEM), which incorporates the SRTM DEM in areas where SRTM is available,
529  such as Austria (Kääb et al. 2016). The geometric accuracy of the Sentinel data hence depends on the accuracy of the
530  underlying DEM, which is subject to a number of uncertainties particularly over mountainous terrain. Vertical
531  inaccuracies – which propagate into horizontal inaccuracies - increase over glacier surfaces, especially in areas with
532  large changes in surface elevation, as the DEM can only provide a snapshot of conditions for a moment in time and
533  quickly becomes outdated in rapidly changing environments. Pandžic et al (2016) determine an average offset in the
534  Sentinel-2 data for Austria of about 6m compared to a high-resolution regional DEM. The performance requirement of
535  Landsat-8 OLI for geometric terrain corrected accuracy is specified as 12m (Storey et al, 2014). Kääb et al. (2016) find
536  cross-track offsets of 20-30 m over glacier termini in the Swiss Alps when comparing Landsat-8 and Sentinel-2 scenes
537  acquired on September 8, 2015. Accordingly, uncertainties regarding the GPS points of the in situ measurements as
538  delineated in our sensitivity analysis (Table 4, Figure 11) can be considered relatively small compared to the those
539  related to the orthorectification of the satellite data. Comparisons between in situ point data and pixel values from the
540  satellite products must be interpreted keeping positional uncertainties in mind.

541  Decreasing the pixel resolution and averaging over multiple in situ measurement points can serve as an approach to
542  reduce the influence of geometric errors. However, any sort of averaging procedure must also be assessed in terms of
543  spatial representativeness of the point measurements for a greater area and, conversely, the down sampled satellite data
544  for small scale surface processes. What can be considered representative will always be a question of scale and
545  application. The glacier surface at the study site is locally very heterogenous and hence prone to representativeness
546  errors (Wu et al., 2019). We selected the location of the in situ profile lines so that they cover what we consider to be the
547  typical surface features and types of a given section of the ablation zone and argue that our 20 m long profile lines with
548  equidistant measurements at least every two meters capture any variations that are likely to influence the corresponding
549  pixel values of the satellite data. Naturally, the less overlap there is between the profile lines and any given satellite
550  pixel, the more likely it is that the in situ point data happen to capture something that differs strongly from what the
551  satellite sees.

19

The different surface types identified at Jamtalferner (Fig. 4) and their reflectance spectra are comparable to types of surfaces identified in Switzerland at Morteratsch and Glacier de la Plaine Morte by Di Mauro et al. (2017) and Naegeli et al. (2015), respectively, supporting the use of a classification scheme based on differentiating between a) clean and dirty ice surfaces and b) the presence or absence of liquid water on the ice surface. Classifying the surface characteristics into discrete types can help to ensure representativeness e.g. by quantifying how much of a given area subsection relevant to the comparison with remote sensing data is comprised of which type and then sampling accordingly. However, surface types are not always discrete in practice. Nicholson and Benn (2006) indicate that the surface albedo of ice with scattered debris can be simulated in a modelling approach be linearly varying between clean ice albedo values and values for debris, but this does not necessarily account for other types of surfaces and even the clean ice albedo can vary considerably, especially if liquid water is present. Additionally, classification by type of any kind cannot address the issue of temporal representativeness unless the temporal variability of different surface types is first determined.

Profile 8 shows particularly poor agreement with the corresponding satellite data and may be an example where temporal variability plays a role: The profile crosses a section of ice where the contrast between dark and bright areas is comparatively strong. The profile line is roughly at a right angle to the flow direction of the glacier and "stripes" of meltwater channels and/or dirt cross the line. The profile has a comparable number of individual spectra with reflectance values above and below the profile mean, i.e. it is not a dark profile with a few bright outliers (compare e.g. to P6 in Fig. 6) or vice versa (e.g. P3), but alternates along the profile line. Agreement with the remote sensing data is decent for the darker spectra in P8 but the bright values are not captured. While we cannot rule out that the lack of agreement between the field and remote sensing data is due to an unusually unfortunate/unrepresentative positioning of the field measurement points in the satellite pixels, this may be an instance where the diurnal melt cycle and the associated presence/absence of water on the surface exacerbates the contrast between the dark and bright sections of the profile. In the bright sections, the porous weathering crust and cryconite hole structures appear to be drained of water, while the depressions of the melt channels are noticeably wet. Cook et al. (2016) indicate the occurrence of "sudden drainage events" in the weathering crust on a day-to-day time scale and a diurnal cycle of the hydrology of the weathering crust driven by meteorological conditions (radiation, turbulent fluxes). The time of day of a satellite overpass would determine which stage of this cycle the satellite sees and consequently the satellite data would not capture this variability. In order to assess how much the time of day of the overpass could systematically affect the representativeness of the satellite date for actual ground reflectance, it needs to be determined how significant and how consistent the diurnal cycle is. To do this, the driving processes must be identified, keeping in mind that these may be different for different types of glaciers and that different causes of short-term albedo change can overlap. E.g.: Azzoni et al. (2016) point out that meltwater increases albedo around midday in a daily cycle, while rain causes increased albedo for up to 4 days after the precipitation event. A seasonal cycle of albedo has been demonstrated in previous observational studies and modelling efforts of broadband albedo, highlighting the importance of continuous measurements (e.g. Hoinkes and Wendler, 1968; Nicholson and Benn, 2012; Möller and Möller, 2017).

### 4.3. Relevance of small-scale variability

The reflectance properties of ice are a central part of mass and energy balance modelling, usually in the form of a glacier wide broadband albedo, or using one value for ice in the ablation zone and one for snow covered areas. Resolving local albedo variations at a very small, sub-pixel scale is not required for regional or global studies, provided the albedo parametrization captures the conditions on the ground adequately for the region of interest. In their important 2015 study, Naegeli et al. find that Sentinel-2 and Landsat-8 reflectance data are within the suggested accuracy requirements for global climate modelling (±0.05, Henderson-Sellers and Wilson, 1983) over their study site, Glacier de la Plaine Morte in Switzerland. In the same study, they report a 10% difference in modelled mass balance when a spatially distributed albedo is used to force the model as opposed to a single, glacier wide albedo. Significantly larger differences occur in parts of the glacier where water is present on the surface or the ice surface contains a lot of light-absorbing impurities. While the glacier-wide impact of a spatially distributed albedo on model results may be relatively small, this highlights that resolving local variability of reflectance properties and its causes is important for accurately predicting the future evolution of individual glaciers, especially in cases where the firn covered area is gone or greatly reduced and rapid melt is occurring. Only once the problem of different scales comparing point and spatially averaged data is solved, the relationship between albedo variability and mass balance point and averaged data can be tackled to calculate the effects on mass balance at glacier-wide or regional scale.

Aside from directly mass and energy balance related applications, reflectance data with high spatial and temporal resolution is essential to improve understanding of micro-hydrological processes in the weathering crust and how these

20

may affect a possible larger scale darkening of increasingly snow free glaciers, e.g. by favoring or impeding the growth of ice algae, or the collection/washing out of cryoconite or other impurities. High resolution time series of spectral reflectance at representative locations in the ablation zone are needed to assess how changes in wetness and temperature, surface texture (cryoconite formation, roughness changes during the season), biotic productivity, deposition of sediment by melt water and rain affect reflectance properties on a small spatial scale, throughout the day and over the course of the ablation season. Establishing measurement efforts aimed at generating such time series on glaciers with existing mass balance monitoring networks would be highly desirable in order to better link small scale surface processes with mass and energy balance modelling.

**5. Conclusion & Outlook**

In comparing our in situ measurements with readily available L2A satellite products, we chose an "as simple as possible" approach to gain a general understanding of where sources of uncertainties are. We found that the difference between in situ and satellite data is not uniform across satellite bands, between Landsat and Sentinel, and to some extent between surface types. Reflectance variability on the ground is not fully represented in the satellite data, which raises questions as to how well surface processes at rapidly changing glaciers such as Jamtalferner can be resolved with satellite data.

The reflectance properties of ice, along with other feedback mechanisms such as changing topography and glacier geometry, significantly impact the rate of glacial retreat, contributing to the non-linear characteristics of glacier change and the high variability of defining parameters such as mass-balance or area change even among neighbouring glaciers subject to common climatic drivers (Charalampidis et al., 2018). Understanding these feedback mechanisms and associated processes is key to successfully predicting future glacier changes across spatial and temporal scales. Ice albedo will remain a significant source of uncertainty in modelling applications as long as the processes governing temporal and spatial variability are not fully understood.

Quantifying spatial and temporal variability of spectral reflectance and delineating the main causes of this variability for individual glaciers will improve modelling capabilities of glacier evolution and catchment hydrology. Satellite-derived reflectance products are a key component of tackling similar questions on the regional and global level. However, ground truth data from representative sites is essential in order to understand uncertainties associated with satellite albedo and surface reflectance products and potentially improve them for specific contexts.

Moving forward, an expansion of the monitoring network at Jamtalferner and, ideally, other glaciers, by continuous reflectance measurements in the ablation zone at a fixed location is needed, as well as "snap-shot" measurements of spectral, multi-angular reflectance at multiple strategic points in regular intervals. Combining analysis of spectral reflectance data from in situ and remote sensing sources with the wealth of contextual information available at Jamtalferner and other established monitoring sites has the potential to greatly improve our understanding of the complex interplay of surface changes, glacier dynamics, and mass- and energy balance.

**Author Contribution**

L. Felbauer and A. Fischer collected the in situ data. Subsequent data curation was carried out by L. Felbauer and L. Hartl. G. Schwaizer conceptualized the comparison of in situ and satellite derived data. L. Hartl developed the code for data analysis and visualizations, and wrote the manuscript with contributions from all co-authors.

21

**References**

Alexander, P. M., Tedesco, M., Fettweis, X., Van De Wal, R., Smeets, C. J. P. P., and Van Den Broeke, M. R.: Assessing spatio-temporal variability and trends in modelled and measured Greenland Ice Sheet albedo (2000-2013), The Cryosphere, 8(6), 2293-2312, 2014.

ASD Inc.: FieldSpec® HandHeld2™ Spectroradiometer User Manual. https://www.malvernpanalytical.com/en/support/product-support/asd-range/fieldspec-range/handheld-2-hand-held-vnir-spectroradiometer#manuals, Accessed: Sep. 22, 2020.

Azzoni, R. S., Senese, A., Zerboni, A., Maugeri, M., Smiraglia, C., and Diolaiuti, G. A.: Estimating ice albedo from fine debris cover quantified by a semi-automatic method: the case study of Forni Glacier, Italian Alps, The Cryosphere, 10, 665-679, 2016.

Box, J. E., Fettweis, X., Stroeve, J. C., Tedesco, M., Hall, D. K., and Steffen, K.: Greenland ice sheet albedo feedback: thermodynamics and atmospheric drivers, The Cryosphere, 6(4), 821-839, 2012.

Box J. E., van As D., and Steffen, K. Greenland, Canadian and Icelandic land-ice albedo grids (2000–2016). Geological Survey of Denmark and Greenland Bulletin, 38, 53-56, 2017.

Brun, F., Dumont, M., Wagnon, P., Berthier, E., Azam, M. F., Shea, J. M., Sirguey, P., Rabatel, A., and Ramanathan, A.: Seasonal changes in surface albedo of Himalayan glaciers from MODIS data and links with the annual mass balance, The Cryosphere, 9(1), 341-355, 2015.

Charalampidis, C., Fischer, A., Kuhn, M., Lambrecht, A., Mayer, C., Thomaidis, K., and Weber, M.: Mass-budget anomalies and geometry signals of three Austrian glaciers, Frontiers in Earth Science, 6, p. 218, 2018.

Claverie, M., Ju, J., Masek, J.G., Dungan, J.L., Vermote, E.F., Roger, J.C., Skakun, S.V. and Justice, C.: The Harmonized Landsat and Sentinel-2 surface reflectance data set. Remote sensing of environment, 219, pp.145-161, 2018.

Cook, J.M., Hodson, A.J. and Irvine-Fynn, T.D.: Supraglacial weathering crust dynamics inferred from cryoconite hole hydrology. Hydrological Processes, 30(3), pp.433-446, 2016.

Dirmhirn, I. and Trojer, E.: Albedountersuchungen auf dem Hintereisferner, Archiv für Meteorologie, Geophysik und Bioklimatologie, Serie B, 6(4), pp.400-416, 1955.

Dumont, M., Brun, E., Picard, G., Michou, M., Libois, Q., Petit, J. R., Geyer, S., and Josse, B.: Contribution of light-absorbing impurities in snow to Greenland's darkening since 2009, Nature Geoscience, 7(7), 509, 2014.

Fischer, A.: Comparison of direct and geodetic mass balances on a multi-annual time scale. The Cryosphere, 5, pp.107-124, 2011.

Fischer, A., Helfricht, K., Wieseneger, H., Hartl, L., Seiser, B., and Stocker-Waldhuber, M.: Chapter 9 - What Future for Mountain Glaciers? Insights and Implications From Long-Term Monitoring in the Austrian Alps, in: Developments in Earth Surface Processes, edited by: Greenwood, G., B. and Shroder, J. F., Elsevier, 21, 325-382, 2016.

Fischer, A., Markl, G., and Kuhn, M.: Glacier mass balances and elevation zones of Jamtalferner, Silvretta, Austria, 1988/1989 to 2016/2017, Institut für Interdisziplinäre Gebirgsforschung der Österreichischen Akademie der Wissenschaften, Innsbruck, PANGAEA, https://doi.org/10.1594/PANGAEA.818772, 2016.

Fischer, A., Fickert, T., Schwaizer, G., Patzelt, G. and Groß, G.: Vegetation dynamics in Alpine glacier forelands tackled from space, Scientific reports, 9(1), pp.1-13, 2019.

Gabbi, J., Huss, M., Bauder, A., Cao, F., & Schwikowski, M.: The impact of Saharan dust and black carbon on albedo and long-term mass balance of an Alpine glacier, The Cryosphere, 9(4), 1385-1400, 2015.

Gardner, A. S. and Sharp, M. J.: A review of snow and ice albedo and the development of a new physically based broadband albedo parameterization, Journal of Geophysical Research: Earth Surface, 115(F1), 2010.

22

716  GeoPandas developers: GeoPandas 0.8.0. URL: https://geopandas.org/, 2013-2019. Accessed: 2020.
717
718  Gillies, S., & others. (n.d.). Rasterio: Geospatial raster i/o for Python programmers. Mapbox, 2013. Retrieved from
719  https://github.com/mapbox/rasterio, 2020.
720
721  Gorelick, N., Hancher, M., Dixon, M., Ilyushchenko, S., Thau, D., and Moore, R.: Google Earth Engine: Planetary-scale
722  geospatial analysis for everyone, Remote Sensing of Environment, 202, pp.18-27, 2017.
723
724  Greuell, W. and de Wildt, M.D.R.: Anisotropic reflection by melting glacier ice: Measurements and parametrizations in
725  Landsat TM bands 2 and 4. Remote Sensing of Environment, 70(3), pp.265-277, 1999.
726
727  Hall, D. K., Chang, A. T. C., Foster, J. L., Benson, C. S., and Kovalick, W. M.: Comparison of in situ and Landsat
728  derived reflectance of Alaskan glaciers, Remote Sensing of Environment, 28, 23-31, 1989.
729
730  Hall, D. K., Bindschadler, R. A., Foster, J. L., Chang, A. T. C., and Siddalingaiah, H.: Comparison of in situ and
731  satellite-derived reflectances of Forbindels Glacier, Greenland, Remote Sensing, 11(3), 493-504, 1990.
732  Hall, D.: Remote sensing of ice and snow, Springer Netherlands, 2012.
733
734  Henderson-Sellers, A. and Wilson, M.F.: Surface albedo data for climatic modeling. Reviews of Geophysics, 21(8),
735  pp.1743-1778, 1983.
736  Hendriksa J, Pellikkaa P, Peltoniemib J. Estimation of anisotropic radiance from a glacier surface-Ground based
737  spectrometer measurements and satellite-derived reflectances. In Proceedings, 30th International Symposium on
738  Remote Sensing of Environment: Information for Risk Management and Sustainable Development, November 10-14,
739  Honolulu, Hawaii, 2003.
740
741  Hoinkes, H., and Wendler, G.: Der Anteil der Strahlung an der Ablation von Hintereis-und Kesselwandferner (Ötztaler
742  Alpen, Tirol) im Sommer 1958, Archiv für Meteorologie, Geophysik und Bioklimatologie, Serie B, 16(2-3), 195-236,
743  1968.
744
745  Hunter, J.D.: Matplotlib: A 2D Graphics Environment, Computing in Science & Engineering, 9, 90-95, 2007.
746
747  Jaffé, A.: Über Strahlungseigenschaften des Gletschereises, Archiv für Meteorologie, Geophysik und Bioklimatologie,
748  Serie B, 10(3), pp.376-395, 1960.
749
750  Kääb, A., Winsvold, S.H., Altena, B., Nuth, C., Nagler, T. and Wuite, J.: Glacier remote sensing using Sentinel-2. part I:
751  Radiometric and geometric performance, and application to ice velocity. Remote Sensing, 8(7), p.598, 2016.
752  Klok, E.L., Greuell, W. and Oerlemans, J.:Temporal and spatial variation of the surface albedo of Morteratschgletscher,
753  Switzerland, as derived from 12 Landsat images. Journal of Glaciology, 49(167), pp.491-502, 2003.
754
755  Knap, W. H., Brock, B. W., Oerlemans, J., and Willis, I. C.: Comparison of Landsat TM-derived and ground-based
756  albedos of Haut Glacier d'Arolla, Switzerland, International Journal of Remote Sensing, 20(17), 3293-3310, 1999.
757  Koelemeijer, R., Oerlemans, J., and Tjemkes, S.: Surface reflectance of Hintereisferner, Austria, from Landsat 5 TM
758  imagery, Annals of Glaciology, 17, 17-22, 1993.
759  Kuhn, M.: The response of the equilibrium line altitude to climate fluctuations: theory and observations, in: Glacier
760  fluctuations and climatic change, 407-417, Springer, Dordrecht, 1989.
761  Lee, Y.: SpecDAL Reference. https://specdal.readthedocs.io/en/latest/, 2017. Accessed: September 2019.
762  Li, Z., Erb, A., Sun, Q., Liu, Y., Shuai, Y., Wang, Z., Boucher, P. and Schaaf, C.: Preliminary assessment of 20-m
763  surface albedo retrievals from sentinel-2A surface reflectance and MODIS/VIIRS surface anisotropy measures. Remote
764  sensing of environment, 217, pp.352-365, 2018.
765  Malinka, A., Zege, E., Heygster, G. and Istomina, L.: Reflective properties of white sea ice and snow. The Cryosphere,
766  10, 2541–2557, 2016.
767
768  Mayer, B. and Kylling, A.: Technical note: The libRadtran software package for radiative transfer calculations -
769  description and examples of use, Atmos. Chem. Phys., 5, 1855-1877, https://doi.org/10.5194/acp-5-1855-2005, 2005.
770

23

771 Main-Knorn, M., Pflug, B., Louis, J., Debaecker, V., Müller-Wilm, U., and Gascon, F.: Sen2Cor for Sentinel-2, in:
772 Image and Signal Processing for Remote Sensing XXIII, International Society for Optics and Photonics, Warsaw,
773 Poland, 11-13 September 2017, Vol. 10427, p. 1042704, 2017.
774
775 McKinney W.: Data structures for statistical computing in python. In: Proceedings of the 9th Python in Science
776 Conference 2010 Jun 28 (Vol. 445, pp. 51-56).
777
778 Nicholson, L. and Benn, D.I.: Properties of natural supraglacial debris in relation to modelling sub-debris ice ablation.
779 Earth Surface Processes and Landforms, 38(5), pp. 490-501, 2012.
780
781 Di Mauro, B., Baccolo, G., Garzonio, R., Giardino, C., Massabò, D., Piazzalunga, A., Rossini, M., and Colombo, R.:
782 Impact of impurities and cryoconite on the optical properties of the Morteratsch Glacier (Swiss Alps), The Cryosphere,
783 11(6), 2393, 2017.
784
785 Di Mauro, B., Garzonio, R., Baccolo, G., Franzetti, A., Pittino, F., Leoni, B., Remias, D., Colombo, R. and Rossini, M.:
786 Glacier algae foster ice-albedo feedback in the European Alps. Scientific reports, 10(1), pp.1-9, 2020.
787
788 Ming, J., Du, Z., Xiao, C., Xu, X., and Zhang, D.: Darkening of the mid-Himalaya glaciers since 2000 and the potential
789 causes, Environmental Research Letters, 7(1), 014021, 2012.
790
791 Ming, J., Wang, Y., Du, Z., Zhang, T., Guo, W., Xiao, C., Xu, X., Ding, M., Zhang, D., and Yang, W.: Widespread
792 albedo decreasing and induced melting of Himalayan snow and ice in the early 21st century, PLoS One, 10(6),
793 e0126235, 2015.
794
795 Moller, M. and Moller, R.: Modeling glacier-surface albedo across Svalbard for the 1979–2015 period: The
796 HiRSvaC500-a data set. J. Adv. Model. Earth Syst., 9, 404– 422, 2017.

797 Naegeli, K., Damm, A., Huss, M., Schaepman, M., and Hoelzle, M.: Imaging spectroscopy to assess the composition of
798 ice surface materials and their impact on glacier mass balance, Remote Sensing of Environment, 168, 388-402, 2015.
799
800 Naegeli, K. and Huss, M.: Mass balance sensitivity of mountain glaciers to changes in bare-ice albedo. Annals of
801 Glaciology, No. 75, The Cryosphere in a Changing Climate, 2017.
802
803 Naegeli, K., Damm, A., Huss, M., Wulf, H., Schaepman, M., and Hoelzle, M.: Cross-Comparison of albedo products for
804 glacier surfaces derived from airborne and satellite (Sentinel-2 and Landsat 8) optical data, Remote Sensing, 9(2), 110,
805 2017.
806
807 Naegeli, K., Huss, M. and Hoelzle, M.: Change detection of bare-ice albedo in the Swiss Alps, The Cryosphere, 13(1),
808 397-412, 2019.
809
810 Nicodemus, F.E., Richmond, J.C., Hsia, J.J., Ginsberg, I.W. and Limperis, T.: Geometrical considerations and
811 nomenclature for reflectance, Vol. 160. Washington, DC: US Department of Commerce, National Bureau of Standards,
812 1977.
813
814 Oerlemans, J.: Glaciers and climate change. CRC Press, 2001.

815 Oerlemans, J., R. H. Giesen, and M. R. Van den Broeke: Retreating alpine glaciers: increased melt rates due to
816 accumulation of dust (Vadret da Morteratsch, Switzerland), Journal of Glaciology, 55, no. 192, 729-736, 2009.
817
818 Painter, T. H., Flanner, M. G., Kaser, G., Marzeion, B., VanCuren, R. A., and Abdalati, W.: End of the Little Ice Age in
819 the Alps forced by industrial black carbon, Proceedings of the National Academy of Sciences, 110(38), 15216-15221,
820 2013.
821
822 Pandzić, M., Mihajlović, D., Pandzić, J. and Pfeifer, N.: Assessment of the geometric quality of sentinel-2 data. In
823 XXIII ISPRS Congress, Commission I, Vol. 41, No. B1, 489-494. International Society for Photogrammetry and
824 Remote Sensing, 2016.
825
826 Paul, F., Machguth, H., and Kääb, A.: On the impact of glacier albedo under conditions of extreme glacier melt: the
826 summer of 2003 in the Alps, EARSeL eProceedings, 4(2), 139-149, 2005.

24

Qu, B., Ming, J., Kang, S. C., Zhang, G. S., Li, Y. W., Li, C. D., Zhao, S.Y., Ji, Z. M., and Cao, J. J.: The decreasing albedo of the Zhadang glacier on western Nyainqentanglha and the role of light-absorbing impurities, Atmospheric Chemistry and Physics, 14(20), 11117-11128, 2014.

Richter, R. and Schläpfer, D.: Atmospheric/Topographic Correction for Satellite Imagery: ATCOR-2/3 UserGuide", DLR IB 565-01/11, Wessling, Germany, 2011.

Rhodes, B.: PyEphem. URL: https://rhodesmill.org/pyephem/toc.html, 2020.

Sauberer, F.: Versuche über spektrale Messungen der Strahlungseigenschaften von Schnee und Eis mit Photoelementen, Meteorol. Z., 55, 250, 1938.

Sauberer, F. and Dirmhirn, I.: Untersuchungen über die Strahlungsverhältnisse auf den Alpengletschern, Archiv Met. Geoph. Biokl. Ser. B.3, 256, 1951.

Sauberer, F. And Dirmhirn, I.: Der Strahlungshaushalt horizontaler Gletscherflächen auf dem Hohen Sonnblick, Geogr. Ann., 34, 261, 1952.

Schaepman-Strub, G., T. Painter, S. Huber, S. Dangel, M. E. Schaepman, J. Martonchik, and F. Berendse.: About the importance of the definition of reflectance quantities-results of case studies. In: Proceedings of the XXth ISPRS Congress, 361-366, 2004.

Schaepman-Strub, G., Schaepman, M. E., Painter, T. H., Dangel, S., and Martonchik, J. V.: Reflectance quantities in optical remote sensing—Definitions and case studies. Remote sensing of environment, 103(1), 27-42, 2006.

Shuai, Y., Masek, J.G., Gao, F. and Schaaf, C.B.: An algorithm for the retrieval of 30-m snow-free albedo from Landsat surface reflectance and MODIS BRDF. Remote Sensing of Environment, 115(9), 2204-2216, 2011.

Storey, J., Choate, M. and Lee, K.: Landsat 8 Operational Land Imager on-orbit geometric calibration and performance. Remote sensing, 6(11), 11127-11152, 2014.

U.S. Geological Survey: Landsat 8 Collection 1 (C1) Land Surface Reflectance Code (LaSRC) Product Guide Version 3.0, 2020. https://www.usgs.gov/media/files/landsat-8-collection-1-land-surface-reflectance-code-product-guide Accessed: September 17, 2020.

van As, D., Fausto, R. S., Colgan, W.T., and Box, J.E.: Darkening of the Greenland ice sheet due to the melt albedo feedback observed at PROMICE weather stations. Geological Survey of Denmark and Greenland (GEUS) Bulletin 28:69-72, 2013.

Van de Wal, R.S.W., Oerlemans, J., and Van der Hage, J.C.: A study of ablation variations on the tongue of Hintereisferner, Austrian Alps, Journal of Glaciology, 38(130), pp.319-324, 1992.

Van der Walt, S., Colbert, C., and Varoquaux, G.: The NumPy Array: A Structure for Efficient Numerical Computation, Computing in Science & Engineering, 13, 22-30, 2011.

Van Rossum, G., Drake, F.L.: Python 3 Reference Manual. Scotts Valley, CA: CreateSpace; 2009.

Vermote, E., Justice, C., Claverie, M., and Franch, B.: Preliminary analysis of the performance of the Landsat 8/OLI land surface reflectance product, Remote Sensing of Environment, 185, 46-56, 2016.

Winther, J. G.: Landsat TM derived and in situ summer reflectance of glaciers in Svalbard, Polar Research,12(1), 37-55, 1993.

Wu, X., Wen, J., Xiao, Q., You, D., Lin, X., Wu, S. and Zhong, S.: Impacts and Contributors of Representativeness Errors of In Situ Albedo Measurements for the Validation of Remote Sensing Products. IEEE Transactions on Geoscience and Remote Sensing, 57(12), 9740-9755, 2019

Zemp, M., Frey, H., Gärtner-Roer, I., Nussbaumer, S.U., Hoelzle, M., Paul, F., Haeberli, W., Denzinger, F., Ahlstrøm, A.P., Anderson, B., and Bajracharya, S.: Historically unprecedented global glacier decline in the early 21$^{st}$ century, Journal of Glaciology, 61(228), 745-762, 2015.

884 Zemp, M., Huss, M., Thibert, E., Eckert, N., McNabb, R., Huber, J., Barandun, M., Machguth, H., Nussbaumer, S.U.,
885 Gärtner-Roer, I. and Thomson, L.: Global glacier mass changes and their contributions to sea-level rise from 1961 to
886 2016, Nature, 568(7752), 382-386, 2019.

887 Zeng, Q., Cao, M., Feng, X., Liang, F., Chen, X., and Sheng, W.: A study of spectral reflection characteristics for snow,
888 ice and water in the north of China, Hydrological applications of remote sensing and remote data transmission, 145,
889 451-462, 1984.

890